

See discussions, stats, and author profiles for this publication at: <https://www.researchgate.net/publication/231659546>

Photoinduced Near Ultraviolet Three Body Decay of Phosgene

ARTICLE *in* THE JOURNAL OF PHYSICAL CHEMISTRY A · SEPTEMBER 1997

Impact Factor: 2.69 · DOI: 10.1021/jp970741v

CITATIONS

22

READS

13

3 AUTHORS, INCLUDING:



Christof Maul

Technische Universität Braunschweig

58 PUBLICATIONS 648 CITATIONS

SEE PROFILE



Karl-Heinz Gericke

Technische Universität Braunschweig

171 PUBLICATIONS 2,471 CITATIONS

SEE PROFILE

Photoinduced Near Ultraviolet Three Body Decay of Phosgene

Christof Maul, Tobias Haas, and Karl-Heinz Gericke*

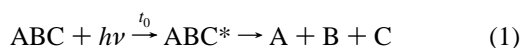
*Institut für Physikalische und Theoretische Chemie der Technischen Universität,
Hans-Sommer-Strasse 10, D-38106 Braunschweig, Germany*

Received: February 27, 1997; In Final Form: April 11, 1997[⊗]

Faced with the problem of underdetermined kinetic equations in analyzing momenta and kinetic energies of three body decay fragments, we followed two conceptually different paths in order to shed light on the dynamics of the process. One is based on the evaluation of the observed kinematic quantities after introduction of physically meaningful parameters for each type of decay: sequential, synchronously concerted, and asynchronously concerted mechanism. The other one is based on an information theoretic approach, maximizing the entropy of the joint probability matrix containing the probabilities for coincidentally realizing accessible sets of product states. The results obtained in both cases match remarkably well: No significant contribution of a molecular channel, producing chlorine molecules, was found. Likewise, the generation of a stable chloroformyl radical had been ruled out in previous studies, so that every dissociation process upon irradiation around 230 nm yields three fragments: two chlorine atoms and a carbon monoxide molecule. For this three body decay, the asynchronously concerted mechanism is the dominant dissociation channel, accounting for over 80% of the products. The chlorine fragments move preferentially in the same direction, resulting in forward scattering of the carbon monoxide. A less abundant decay channel is the synchronously concerted mechanism, in which the two bonds cleave in unison, and that accounts for the remaining products. The geometry of the decaying parent resembles the ground state equilibrium geometry with significant excitations of the COCl₂ bending modes. For both mechanisms the CO fragments are generated with high internal excitation.

I. Introduction

The three body breakup of a molecule upon irradiation and photon absorption is the easiest example of a concerted chemical reaction, where concertedness in this context means the breaking of different chemical bonds in a single kinetic event in contrast to a sequence of individual reactions.¹ Generally speaking, this process can be expressed by the following simple reaction mechanism:



where a molecule ABC is excited by absorbing a photon $h\nu$ at time t_0 and subsequently decays into three particles A, B, and C. A, B, and C merely represent any final fragments without implying that these fragments be atomic. B in this context always denotes the central particle bound to both A and C. The simplicity of such a system allows one to obtain insight into the dynamics of concerted bond-breaking in a molecule. Therefore, studying three body processes is of fundamental interest in the field of reaction dynamics. Apart from this fundamental aspect the results are significant for understanding complex reaction schemes where the encounter of three collision partners is a crucial step in numerous processes governing, e.g., chemical reactions in the atmosphere or in combustion.

For a long time the study of three body decays has been regarded as a more or less exotic subject and more often than not has only been considered in the literature in order to explain unwanted effects obscuring the desired information. However, due to improved experimental and theoretical tools, over the last few years there has been a dramatic increase in the number of studies devoted to the investigation of three body decays as

such, and only very recently the work in this field has extensively been reviewed.²

Some technical terms used in discussing concertedness have been used in a nonmatching, or worse, contradictory manner by different authors. In order to avoid misunderstandings we want to clarify our choice of vocabulary: A concerted decay will take place in a single kinetic event as opposed to a sequential decay, which is characterized by a sequence of two independent dissociative steps, with the decay of AB not being influenced by forces from the first fragment C. Here a kinetic event is defined by a molecular clock referring to the mean rotational period τ_{rot} of the primary intermediate decay product. The preference for using the rotational criterion over the vibrational one has been discussed previously.² Thus, a three body decay will be called sequential, if the time span $\Delta t = t_2 - t_1$ between the times t_1 and t_2 of the first and second bond cleavages is greater than the mean rotational period of the primary fragment AB: $\Delta t > \tau_{\text{rot}}$. Then eq 1 becomes



where the asterisks indicate particles with internal excitation above their dissociation thresholds with respect to the separation into the final ground state fragments. Consequently, apart from conservation of total angular momentum, the decaying primary fragment AB* at time t_2 does not carry any memory of the orientation of the excited parent ABC* at time t_1 , and the energy partitioning in the final fragments for a given set of quantum states will be determined by the conservation laws only.

For smaller values of Δt ($\Delta t \leq \tau_{\text{rot}}$) the two decay processes are no longer independent of each other, and such a memory will be preserved. Then the additional geometrical constraint on the final products leads to an energy partitioning in the fragments that is characteristic of the decay process. Thus,

[⊗] Abstract published in *Advance ACS Abstracts*, July 15, 1997.

different decay mechanisms producing chemically identical products A, B, and C in identical quantum states can be distinguished by the energy content and the spatial distribution of the products. For vanishing Δt the process will be called synchronously concerted in order to distinguish it from the asynchronously concerted decay with $0 < \Delta t \leq \tau_{\text{rot}}$. This concept of synchronicity implies that the linear momenta transferred into the fragments A and C be identical.

A very illustrative, yet oversimplifying picture of synchronously and asynchronously concerted mechanisms are decays via symmetric and antisymmetric stretching modes of a linear ABA parent molecule, respectively. Adopting this simple view, the excitation of the symmetric stretching mode lengthens both bonds A–B in phase and causes both fragments to be ejected from the parent at exactly the same time: $\Delta t = 0$, which is characteristic for a synchronous decay. The excitation of the antisymmetric stretching mode with vibrational period τ_{vib} , however, leads to the lengthening of one bond along with the contraction of the other one. Hence the oscillations in bond length are phase-shifted against each other by 180° , and the departure of the second fragment will take place half a vibrational period later than the first one: $\Delta t = \tau_{\text{vib}}/2$, which is characteristic of an asynchronous decay. Then the energy transfer for the two fragments is different because of the different masses of the respective “collision partners”.

While the analysis of a two body decay,



can be performed in a straightforward manner, the corresponding analysis of a three body decay is by far more complex due to underdetermined kinetic equations. For the regular two body photodissociation one obtains, based on the evaluation of the energy balance in the center of mass frame of the parent molecule XY,

$$E_{\text{av}} = E(XY) + h\nu - D_0(X-Y) = E(X) + T(X) + E(Y) + T(Y) \quad (4)$$

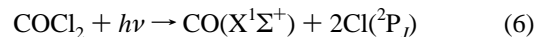
E representing the internal energies of the parent molecule and of the fragments prior to and after the decay, respectively, T the kinetic energies of the fragments, $h\nu$ the photon energy, and D_0 the dissociation energy of the parent. The available energy E_{av} is given by the sum of the well-characterized quantities on the left hand side of eq 4. Observing one fragment by a state-selective, kinetic energy sensitive method yields E and T of the respective dissociation product, leaving E and T of the partner product as unknown quantities, which are unambiguously determined by the conservation laws for linear momentum and energy.

Analyzing the three body decay (1) equivalently, one has to deal with two additional terms, $E(C)$ and $T(C)$, on the right-hand side of the energy balance equation:

$$E_{\text{av}} = E(A) + T(A) + E(B) + T(B) + E(C) + T(C) \quad (5)$$

Performing the same experiment as for the two body case yields two energy values, e.g., $E(A)$ and $T(A)$, but now one is left with four unknown quantities on the right-hand side of eq 5, only two of which are determined by the conservation laws. Since additional experimental information is difficult to obtain, requiring coincidence measurements, one has to introduce dissociation models or make assumptions about partial or complete energy redistribution in the parent molecule prior to its decay. Suitable approaches will be presented in this work, and the employed analysis procedures are briefly outlined in the following section.

Those procedures were applied to the three body decay of phosgene (COCl_2), where upon the absorption of a near-ultraviolet (UV) photon two chlorine atoms and one carbon monoxide molecule in their respective electronic ground states are produced:^{3,4}



This system is ideally suited for studying a three body decay process for many reasons. All products are spectroscopically accessible to experimental observation. They do not possess too many internal degrees of freedom. The generation of atomic fragments facilitates the applicability of the decay model as presented below. Additionally, since only little is known about primary photoproducts from reaction 6, the results are of great significance for tropospheric and stratospheric chemistry.^{5–7}

The geometry of the ground state of phosgene is well-characterized. It is planar with the central carbon atom doubly bound to the oxygen atom and singly bound to the two chlorine atoms. The ground state is of 1A_1 symmetry and belongs to the C_{2v} point group. Being the fully chlorinated analogue to formaldehyde (H_2CO) it also resembles the acetone molecule ($(\text{CH}_3)_2\text{CO}$), both of which are by far better characterized with respect to photochemical behavior. The C=O bond length $r_{\text{C=O}}$ is 111.6 ± 0.2 pm, the C–Cl bond length $r_{\text{C–Cl}}$ is 174.6 ± 0.4 pm, and the Cl–C–Cl bond angle $\alpha_{\text{Cl–C–Cl}}^0$ is $111.3 \pm 0.1^\circ$.^{8,9} The rotational constants have been determined to be $A = 0.08049 \pm 0.00002$ cm^{–1}, $B = 0.11675 \pm 0.00002$ cm^{–1}, and $C = 0.26423 \pm 0.00001$ cm^{–1}.⁸ The vibrational energies lie between 285 and 1827 cm^{–1}. The softest mode is the Cl–C–Cl bending mode, while the strongest one is the C=O stretching mode.^{10–15} In order to limit the number of populated states of the parent molecule prior to the absorption of the dissociating photon, experiments must be performed under the low temperature conditions of a supersonic jet. However, the remaining rotational excitation, while insignificant energetically, needs to be taken into account in an angular momentum analysis of the process.

A weak absorption continuum starts at 305 nm with a maximum at 232 nm^{16–20} followed by a much stronger and structureless second continuum below 215 nm.^{21,22} Unlike the formaldehyde case the first continuum is only weakly structured. Featureless vibrational bands dominate the entire range of the first continuum and could be assigned for long wavelengths. These bands are increasingly diffuse for shorter wavelengths, which has been ascribed to a predissociative excited state.

The absorption in this wavelength range excites phosgene from the X^1A_1 electronic ground state into the first electronically excited A^1A_2 state. This symmetry forbidden transition exhibits only a small oscillator strength of $f = 1.04 \times 10^{-3}$, which within molecular orbital theory corresponds to a $\pi^* \leftarrow n$ excitation of a nonbonding electron into an antibonding orbital of the CO bond.²³ Apart from increasing the CO bond length from 116.6 to 132.6 pm and correspondingly reducing the eigenvalue of the CO stretch from 1827 to 1135 cm^{–1}, this excitation induces a nonplanar configuration: the oxygen atom departs from the molecular plane, thus reducing the symmetry group from C_{2v} to C_s . The remaining molecular constants are only insignificantly affected.

The phosgene photodissociation^{24–26} has been investigated by various methods. The quantum yield for $\phi(\text{COCl}_2)$ for the dissociation of phosgene is unity in the entire wavelength range (193–253 nm) under consideration.²² At 253 nm the quantum yield for CO production ϕ_{CO}^{253} is unity.²⁶ By performing end product analysis after adding radical scavengers, a sequential

three body has been postulated, first producing a chloroformyl radical (COCl) and a chlorine atom, the COCl radical further decaying into carbon monoxide and a second chlorine atom.^{24,25} This mechanism has also been suggested from theoretical calculations.²⁷ Recently chlorine atoms were observed in their electronic $^2P_{3/2}$ ground state as primary photoproducts at a photolysis wavelength of 248 nm, but no Cl atoms in the $^2P_{1/2}$ excited spin-orbit state were detectable.⁴ In previous experiments at the slightly shorter photolysis wavelengths of 235 and 237 nm, we observed chlorine atoms both in the $^2P_{3/2}$ ground state (85%) and in the $^2P_{1/2}$ excited spin-orbit state (15%),³ while no evidence for the formation of the chloroformyl (COCl) radical was found. The analysis of the spin polarization and the spin-selective kinetic energy distributions led us to propose an asynchronously concerted mechanism to be active rather than a sequential one, with competing dissociation pathways being responsible for the observed spin-selectivity. We also predicted a significant internal excitation of the carbon monoxide fragments.

Numerous investigations in a broad wavelength range were undertaken to directly address the three body decay of closely related molecules. The dissociation process upon the excitation of the S_2 state of acetone was found to proceed sequentially by first producing a CO molecule and an acetyl radical, which falls apart in an independent second step.^{28,29} A sequential decay was observed upon exciting a Rydberg state in the acetone molecule in the vacuum UV wavelength range around 150 nm,³⁰ and the three body breakup of the acetyl halides was also characterized to follow a sequential mechanism.^{31–35} For the corresponding sulfoxides (thionyl chloride, SOCl₂, and dimethyl sulfoxide, (CH₃)₂SO) the three body decay proceeds concertedly for a dissociation wavelength of 193 nm,^{36–39} but lowering the photon energy for SOCl₂ the decay character seems to change to sequential at a wavelength of 248 nm.³⁷ A significantly more complex behavior has only recently been found for the four body breakup of oxalyl chloride (COCl)₂, where from observing kinetic and internal energies of all final fragments CO and Cl a two-step mechanism was proposed, where a concerted three body decay into CO, Cl, and COCl is followed by the cleavage of the remaining C–Cl bond in a second, independent step.⁴⁰

To complement our previous data on the phosgene three body dissociation, we additionally monitored the CO fragment and treated the observed kinetic energy distributions by kinematic analysis, while the energy distribution of the chlorine atoms was analyzed by a statistical procedure, both of which will be briefly outlined in the following section. A third section will present the experimental setup and observations, followed by a discussion of the results of the analysis procedures and conclusive remarks.

II. Analyzing Procedures

Faced with the problem of underdetermined kinetic equations in analyzing momenta and kinetic energies of three body decay fragments, we followed two conceptually different paths in order to shed light on the dynamics of the process. One is based on the evaluation of the observed kinematic quantities after introduction of physically meaningful parameters for each type of decay: sequential, synchronously concerted, and asynchronously concerted mechanism.^{2,41} The other one is based on an information theoretic approach, maximizing the entropy of the joint probability matrix containing the probabilities for coincidentally realizing accessible sets of product states.^{42,43} These two procedures will be called the kinematic and the statistic approach.

A. Kinematic Analysis Procedure. Within each decay model the kinetic fragment properties and the initially excited state of the parent molecule are unambiguously related for given parameter values. Consequently, a known distribution of parameter values yields a specific kinetic energy distribution for each fragment. Once these relationships are known, the procedure can be reversed: From experimentally observing kinetic energy distributions, one can fit the experimental data by adjusting parameter distributions for the decay mechanism(s). For a rigorous description of the kinematic analyzing procedure, the reader is referred to the literature.²

The synchronous three body decay is to be understood as the process where a particle ABC fragments into the three particles A, B, and C, with the bonds AB and BC breaking strictly simultaneously. Then the momenta transferred onto the particles A and B must be equal to one another and the axis of motion of particle B equally divides the bond angle α . The bond angle, defined as the angle formed by the three particles A, B, and C at the time of fragmentation, is the only parameter necessary to unambiguously describe the synchronous three body decay.

Then the kinetic energies T of all three fragments can be expressed in terms of the bond angle α , the reduced mass μ_{AC} of the two terminating particles A and C, and the total kinetic energy ϵ :

$$\begin{aligned} T_A &= \frac{\epsilon}{4 \frac{m_A}{m_B} \cos^2(\alpha/2) + \frac{m_A + m_C}{m_C}} \\ T_B &= \frac{\epsilon}{1 + \frac{m_B}{4\mu_{AC}} (1 + \tan^2(\alpha/2))} \\ T_C &= \frac{\epsilon}{4 \frac{m_C}{m_B} \cos^2(\alpha/2) + \frac{m_A + m_C}{m_A}} \end{aligned} \quad (7)$$

where

$$\epsilon = E_{av} - \sum_{A,B,C} E_i = \sum_{A,B,C} T_i \quad \text{and} \quad \mu_{AC} = \frac{m_A m_C}{m_A + m_C} \quad (8)$$

For a linear molecule ($\alpha = 180^\circ$) the central particle B will stay at rest, while the kinetic energies for the particles A and C are given by the inverse ratio of their masses:

$$T_A = \epsilon \frac{m_C}{m_A + m_C}, \quad T_B = 0, \quad T_C = \epsilon \frac{m_A}{m_A + m_C} \quad (9)$$

The description of the sequential mechanism is divided into two parts. First, the two decay steps are treated as two independent two body decays according to eq 2. Second, a transformation of the center of mass coordinates of the second step into the laboratory coordinates has to be performed.

Then the energy E_{AB} , the internal energy temporarily deposited in the intermediate particle AB in the first step, which cannot be observed experimentally, governs the distribution of the kinetic energy of the final fragment C as well as influencing the distributions of the kinetic energies for the final fragments A and B. In this context E_{AB} is defined as that portion of the internal energy of AB that exceeds the dissociation energy of AB. This is consistent with the definition of the available energy E_{av} with respect to the three final products A, B, and C in their

respective ground states. The kinetic energy of fragment C is immediately obtained:

$$T_C = \frac{m_{AB}}{m_C} T_{AB} = \frac{m_{AB}}{m_{ABC}} (\epsilon - E_{AB} - E(C)) \quad (10)$$

Since now the second decay step takes place in the moving coordinate system of the intermediate AB particle, as a second parameter the decay angle θ needs to be introduced, which is defined as the angle of the direction of motion of the final fragment A (or B) in the center of mass frame of AB with the direction of motion of the intermediate particle AB in the lab frame. Thus a decay angle $\theta = 0$ describes complete forward scattering, where fragment and center of mass velocities have the same directions, whereas $\theta = \pi$ describes complete backward scattering, where fragment and center of mass velocities have opposite directions.

Then the kinetic energy of A is given in terms of θ and E_{AB} :

$$T_A(E_{AB}, \theta) = p_0(E_i) + M_{AB} E_{AB} + M_\theta \cos \theta (p_2(E_i) + p_1(E_i) E_{AB} - E_{AB}^2)^{1/2} \quad (11)$$

where the following abbreviations have been used

$$\begin{aligned} p_0(E_i) &= \frac{m_A m_C}{m_{AB} m_{ABC}} (\epsilon - E(C)) - \frac{m_B}{m_{AB}} (E(A) + E(B)) \\ p_1(E_i) &= E_{av} - E(C) + E(A) + E(B) \\ p_2(E_i) &= (E(A) + E(B))(E(C) - E_{av}) \\ M_{AB} &= \frac{m_B}{m_{AB}} - \frac{m_A m_C}{m_{AB} m_{ABC}} \\ M_\theta &= 2 \left(\frac{m_A m_B m_C}{m_{AB}^2 m_{ABC}} \right)^{1/2} \end{aligned} \quad (12)$$

Here, the dependence on the parameter values is given explicitly, whereas the contributions of the quantities $E(A)$, $E(B)$, and $E(C)$ that are accessible to experimental observations are combined in the coefficients p_0 , p_1 , and p_2 .

For the fragment B one obtains a formally identical equation by consequently exchanging the masses m_A and m_B , where the coefficients p_0 , M_{AB} , and M_θ have to be correspondingly redefined. By definition of the sequential decay all values for θ ($0 \leq \theta \leq \pi$) are equally probable.

The asynchronously concerted three body decay links the above discussed cases of the synchronous and the sequential decays. One would expect, therefore, that describing the asynchronously concerted mechanism was most easily performed by correspondingly modifying the synchronous model. Although the two concerted mechanisms are close to each other in one's imagination, it is more appropriate to adapt the sequential model and perform necessary alterations. The formalism for describing the synchronous mechanism is not suitable because it makes explicit use of the equality of momentum transfer onto the fragments A and C, a condition that is in general not satisfied for the asynchronous case.

Subsequently the asynchronous decay will be discussed analogously to the sequential decay; i.e., the action of the forces governing the first bond cleavage at time t_1 is supposed to be over when the second bond cleavage takes place at time t_2 . Then, the momenta and the kinetic energies of the final fragments can be described, as is the case for the sequential decay, by introducing the decay angle θ and the energy deposition E_{AB}

as parametric quantities. As before, no other parameter is needed in order to characterize the energy partitioning of the process. This implies that the description of the asynchronously concerted decay is formally identical with the description of the sequential case, and the same eqs 10–12 give the relationship between the fragment kinetic energy and the parameter values not only for the sequential but also for the asynchronously concerted mechanism.

The difference between the two cases is found in the dependence of the second decay step on the first one, such that there remains a memory of the geometry of the parent molecule at time t_1 . For this reason the probability of realizing a certain decay angle is not equally distributed among all possible values as in the sequential case but is determined by the first decay step. Thus, the formalisms describing sequential and asynchronously concerted mechanisms are the same, but the characteristic parameter distributions are different. Consequently, the experimental observation of the kinetic energy distributions, which are unambiguously related to the parameter distribution as described in the following paragraph, allows a distinction between the mechanisms.

The effects of parameter distributions on the probability of observing a certain value for the kinetic energy of a fragment can be determined by using the following general formulas for the relevant cases of one and two parameter quantities:

for 1 parameter

$$f_T(T) = f_1(P_1(T)) \left| \frac{\partial P_1}{\partial T}(T) \right| \quad (13a)$$

for 2 parameters

$$f_T(T) = \int_{L(T)}^{U(T)} dP_2 \left\{ f_2(P_2) f_1(P_1(T, P_2)) \left| \frac{\partial P_1}{\partial T}(T, P_2) \right| \right\} \quad (13b)$$

where the P_i s represent the parameter quantities (decay angle θ , energy deposition E_{AB} , bond angle α), $f_i(P_i)$ s represent the distribution function of the i th parameter, $U(T)$ and $L(T)$ are the energy dependent integration limits for the case of two parameters, and $f_T(T)$ is the kinetic energy distribution of a product. The interdependence of $P_i(T)$ has been derived in the preceding paragraphs.

Thus each fragmentation mechanism induces fragment kinetic energy distributions that are specific for the respective parameter distributions. Vice versa, it is possible to determine the character of the decay mechanism together with the corresponding parameter distribution, having made a few plausible assumptions, as, e.g., Gaussian distributions of the parameter values. Every kinetic energy distribution can be described by the following expression:

$$f_T(T) = A^{\text{syn}} f_E^{\text{syn}}(T, E, \alpha_0, \Delta\alpha) + A^{\text{seq}} f_E^{\text{seq}}(T, E, E_{AB,0}^{\text{seq}}, \Delta E_{AB}^{\text{seq}}) + A^{\text{conc}} f_E^{\text{conc}}(T, E, E_{AB,0}^{\text{conc}}, \Delta E_{AB}^{\text{conc}}, \theta_0, \Delta\theta) \quad (14)$$

where the three discussed decay mechanisms compete in the dissociation process (syn = synchronously concerted; conc = asynchronously concerted; seq = sequential). T and E are quantities that are observable in the experiment. The parameter distributions have been assumed to be Gaussian, centered around $P_{i,0}$ with width ΔP_i . Fitting the right-hand side of eq 14 to the experimentally observed kinetic energy distributions $f_T(T)$ yields the individual contributions A^i of the pure decay mechanisms to the overall process (therefore $\sum A^i = 1$) along with the characteristic decay parameters even in complex cases with competing dissociation mechanisms. The procedure is greatly

facilitated, of course, if only two mechanisms compete, or if a pure mechanism is active.

B. Statistic Analysis Procedure. The details of the statistic analysis procedure have been given elsewhere, so here only the idea will be outlined.^{42,43} The procedure is based on calculating a three dimensional joint probability matrix $P(jkl)$, that contains as elements the probabilities for coincidently realizing certain value triplets $(jkl) = (E_{\text{tot}}(A), E_{\text{tot}}(B), E_{\text{tot}}(C))$ of the total energies $E_{\text{tot}} = E + T$ of the three final fragments A, B, and C. In principle, all degrees of freedom could be considered individually, thus increasing the dimensionality of the matrix, but in order to keep computing feasible and computing time within sensible limits, the reduction to the total energy matrix is appropriate. The joint probability matrix can be obtained from experimental observations by a back projection procedure, by maximizing the entropy and, respectively, by minimizing the information content of the distribution.^{44–46}

The prior distribution $Q(jkl)$, defined as the most probable joint probability matrix, describes the nascent product properties well, if there are no dynamic restrictions active in the decay process. Every element $Q(jkl)$ of the prior matrix is proportional to the number of realization possibilities of the total energy triplet (jkl) . This number is given by multiplying the degeneracies $q(E(i))$ ($i = A, B, C$) of the quantum states of A, B, and C with internal energies $E(A)$, $E(B)$, and $E(C)$ with the density of states $\rho(\epsilon)$ of the total kinetic energy ϵ , summing up over all accessible states, such that the total energy E_{av} is conserved:

$$Q(jkl) = \sum_{E(A)} q(E(A)) \sum_{E(B)} q(E(B)) \sum_{E(C)} q(E(C)) \rho(\epsilon) \delta(T(A), T(B), T(C)) \quad (15)$$

where the δ -function guarantees the conservation of linear momentum. By projecting the prior distribution $Q(jkl)$ onto one total energy axis, one obtains the one-dimensional prior distribution $q(i)$ ($i = j, k, l$) of the total energy of any fragment. If this prior distribution $q(i)$ reflects the experimentally observed energy distribution $p^{\text{exp}}(i)$, the decay proceeds statistically under complete redistribution of the available energy between photon absorption and decay onto all energetically accessible exit channels.

If discrepancies arise between the experimental data $p^{\text{exp}}(i)$ and the prior distribution $q(i)$, the joint probability matrix $P(jkl)$ describing the decay process differs from the prior matrix $Q(jkl)$, and the process is not statistical. Then the correct $P(jkl)$ can be derived from $Q(jkl)$ by introducing Lagrangian multipliers, such that the root mean squares of the difference of the projected $p(i)$ and the experimental distribution $p^{\text{exp}}(i)$ are minimized. Accordingly, the modified joint probability matrix $P(jkl)$ most closely resembles the fully statistical prior matrix $Q(jkl)$ and at the same time reproduces the experimental data $p^{\text{exp}}(E_{\text{tot}}(A))$, $p^{\text{exp}}(E_{\text{tot}}(B))$, and $p^{\text{exp}}(E_{\text{tot}}(C))$. The difference between P and Q is caused by the dynamics of the process.

From conservation of energy and linear momentum, any kinetic energy triplet $(T(A), T(B), T(C))$ can be characterized by an angle χ , which is defined as the angle of the direction of motion of fragment A in the center of mass system of the intermediate AB with the direction of motion of fragment C in the lab coordinate system. If for one fragment, as it is the case for molecules, the total energy E_{tot} can be realized by various value pairs for the internal and kinetic energy, then a given total energy triplet (jkl) is characterized by a corresponding distribution $f^{jkl}(\chi)$, determined by the degeneracies of the respective quantum states. The full distribution $F(\chi)$ is obtained by summing up the individual contributions $f^{jkl}(\chi)$ for all matrix

elements (jkl) . For the prior matrix Q , describing the statistic decay, χ is equally distributed among all possible values between $-\pi$ and $+\pi$:

$$F_Q(\chi) = \sum_{jkl} f^{jkl}(\chi) = \text{const} \quad (16)$$

This statistical angular distribution is changed to nonstatistical, if dynamic constraints are present, and if the decay is described by $P(jkl)$ rather than by $Q(jkl)$:

$$F_P(\chi) = \sum_{jkl} f^{jkl}(\chi) \frac{P(jkl)}{Q(jkl)} \neq \text{const} \quad (17)$$

Apart from characterizing the process as being statistical or not, the angular distribution $F_P(\chi)$ is a direct measure of the spatial fragment distribution. Thus, results obtained by the statistical analysis procedure can directly be compared to the kinematically analyzed data, where decay and bond angle distributions are obtained.

III. Experimental Section

A. Setup. A detailed description of the experimental setup has been given elsewhere.^{41,47} It consists of a home-built single-field time-of-flight (TOF) spectrometer with a ratio of the acceleration to the drift region of 1:2 at a total length of 58 cm. The spectrometer was evacuated to a base pressure of 10^{-4} Pa (10^{-6} mbar) by a 360 L/s turbo molecular pump and a 500 L/s oil diffusion pump. Pure phosgene (Messer Griesheim) was fed into the spectrometer via a supersonic jet, generated in an inductively driven pulsed nozzle (General Valve). The nozzle diameter was 0.5 mm, and the valve was operated at a stagnation pressure of typically 2×10^4 Pa (200 mbar) and a pulse duration of 250 μs , resulting in an operational background pressure of less than 10^{-3} Pa (10^{-5} mbar) at a repetition rate of 10 Hz.

Simultaneous dissociation of phosgene and state-selective detection of CO molecules or Cl atoms were performed by using an excimer laser pumped dye laser (Lambda Physik LPD 3000, Lambda Physik LPX 605i). The dye laser operated with Coumarin-47 at a repetition rate of 10 Hz; its output was frequency doubled by a BBO crystal and focused into the spectrometer. The focal length was 200 mm for CO detection and 60 mm for Cl detection. The laser beam intersected the molecular beam at an angle of 54° , while the spectrometer formed an angle of 90° with the propagation direction of the laser beam. The angle between the spectrometer axis and the electric field vector of the linearly polarized laser light could be varied from 0° to 90° in order to investigate the spatial fragment distribution. The intensity of the laser light and the particle density in the supersonic beam were carefully controlled to avoid kinetic energy transfer onto the fragments due to space charge effects. The laser intensity was typically kept around 200 μJ per pulse. The particle density in the expansion zone was varied in order to investigate the space charge induced distortion of the TOF profiles and was kept well below the onset of Coulomb distortion for the measurements.

The $\text{CO}(X^1\Sigma^+)$ fragments were ionized by resonance-enhanced multiphoton ionization (REMPI), using the $\text{B}^1\Sigma^+$ state as resonant intermediate.^{48,49,51,52} The employed wavelength around 230.1 nm for realizing this (2+1) detection is almost at the maximum of the phosgene absorption spectrum, where it exhibits a cross section of $1.2 \times 10^{-19} \text{ cm}^2$. Under our detection conditions we realized a photon flux of more than 10^{19} photons/pulse $\cdot\text{cm}^2$. As a consequence, both the dissociation and the ionization step were saturated, which was confirmed by the

observation of a quadratic dependence of the ion signal intensity on the laser intensity.

Atomic chlorine was resonantly ionized by a similar (2+1)-REMPI scheme, employing the $4p^2D_{3/2}^0 \leftarrow 3p^2P_{3/2}$ transition at 235.336 nm for ground state atoms and the $4p^2D_{3/2}^0 \leftarrow 3p^2P_{1/2}$ transition at 237.808 nm and the $4p^2D_{1/2}^0 \leftarrow 3p^2P_{1/2}$ transition at 235.205 nm for excited spin-orbit state atoms as resonance enhanced steps.⁵⁰ As for CO, the quadratic dependence of the ion signal intensity on the laser intensity proved the dissociation and the ionization steps to be saturated.³

The experimental performance of the setup was greatly enhanced by operating the system in three modes: (a) the drift mode, (b) the acceleration mode, and (c) the Doppler mode.

In all modes the ions are detected by a double stage multichannel plate assembly (Galileo) with an active diameter of 40 mm. In the drift mode no acceleration field is applied. In this case the spectrometer consists simply of a drift tube with length $s = 58$ cm, and the time of flight t is inversely proportional to the (laboratory) speed v of the ion, $t = s/v$. After passing a discriminator (FAST 7011), the ion signal is monitored by a multihit time to digital converter (FAST 7885) with a time resolution that can be varied from 5 to 80 ns and stored in a data buffer (FAST MCD/PC). Typical acquisition times for a single TOF profile are 3000 s with a total of 3×10^5 ion counts. This mode is highly accurate for determining kinetic energies but insensitive to slow particles due to the velocity component perpendicular to the spectrometer axis superimposed on the fragment velocity by the supersonic jet expansion.

In the acceleration mode the ions are accelerated by a moderate static electric field of typically 10^3 V/m in the acceleration region and detected after passing the drift tube. Here the ions are mass selected, and instead of the total speed v , the measured quantity is the velocity component v_x along the spectrometer axis, monitored by the mass peak broadening. A linear relationship between the velocity component v_x and the deviation Δt from the center t_0 of the time of flight profile holds for our spectrometer geometry:

$$\Delta t = \frac{8t_0^2}{3s} v_x \quad (18)$$

where experimental parameters like the acceleration voltage, the ion mass, and the ion charge are contained in the (experimentally observable) quantity t_0 . Since the velocity component v_x is perpendicular to the velocity of the molecular beam, no laboratory to center of mass transformation has to be performed in this case. The ion signal is monitored by a digital oscilloscope (LeCroy 9450). This procedure is sensitive for all velocities down to zero, but, due to the shorter flight times, the accuracy in the determination of kinetic energies is lower than in the drift mode. Combining the two modes yields experimental data with both high accuracy of the drift mode and completeness of the acceleration mode.

The Doppler mode employs strong acceleration fields in the order of 10^4 V/m in order to assure the arrival of all ions that are generated in one laser pulse at the particle detector. This mode serves for the determination of quantum state populations. Although the Doppler broadening of the spectral lines has not been used for obtaining kinetic energy distributions from the line shape due to the much lower accuracy as compared to the evaluation of the TOF data, it is a most welcome tool to check for the correctness of the kinetic energy distributions, derived from the TOF measurements, by an independent method.

All three operational modes were calibrated with respect to their accuracy in determining kinetic energies by the well-

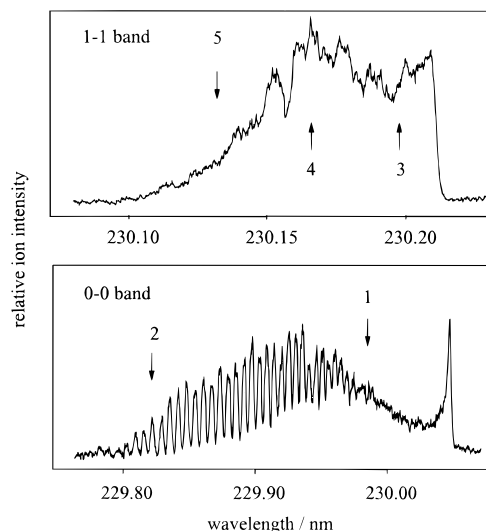


Figure 1. Experimentally observed Q branches of the 0–0 (lower panel) and the 1–1 bands (upper panel) of the $B \leftarrow X$ transition of CO resulting from the photodissociation of phosgene at 230 nm. The intensities have been normalized with respect to the laser power. The rotational overlap in the 1–1 band is due to predissociation of the CO B state in $v = 1$. The arrows mark the states, for which time of flight data have been obtained in order to derive the respective quantum state resolved kinetic energy distributions. The corresponding quantum states are listed in Table 1.

characterized photodissociation of HI^{51-55} at 243 nm and of molecular $Cl_2^{51,52,56-62}$ at 308 nm, monitoring H^{63-65} and $Cl^{50,65,66}$ fragments, respectively. The experimentally determined values are in excellent agreement with the values that were calculated from the spectrometer geometry. The kinetic energy resolution is energy dependent and is approximately 5% for the energy values encountered here, which has experimentally been verified by the Cl_2 dissociation data. Moreover, for the acceleration mode it was carefully checked that data from varied acceleration conditions yielded identical results. For all acquisition modes, immediately after each measurement the background signal was monitored with the laser delayed with respect to the gas pulse under otherwise identical conditions and subtracted from the previously obtained TOF profile. Further data processing was performed by a personal computer.

B. Results. 1. REMPI Spectra of the CO Fragments.

Figure 1 shows the Q branches of the 0–0 and the 1–1 bands of the $CO(B^1\Sigma^+ \leftarrow X^1\Sigma^+)$ transition after normalization with respect to the laser power, observed in the Doppler mode. Very weak O and S branches were also observed, while no P and R branches appear in two-photon $\Sigma \leftarrow \Sigma$ transitions.^{67,68} Intense blue-shaded bandheads are formed because of the very small difference of the rotational constants $B' = 1.912$ cm^{-1} of the B state and $B'' = 1.9313$ cm^{-1} of the ground state. No signal in the wavelength range of the 2–2 band was observed. However, due to the predissociation of the B state of CO for $v' \geq 2$, product generation in higher vibrational states cannot be ruled out. The arrows in Figure 1 mark those transitions for which TOF profiles were obtained in both the acceleration and the drift modes, resulting in (v, J) -state selective kinetic energy distributions of the recoiling CO product. The spectra were recorded by using linearly polarized laser light. Rotating the plane of polarization by 90° with respect to the spectrometer axis did not result in changes of intensities or shapes of single lines or the entire spectrum, confirming the expectations that no such changes should be observed due to the saturation of the dissociation step.

Both vibrational bands exhibit a strong rotational excitation, up to $J'' = 64$ for $v'' = 0$ and $J'' = 55$ for $v'' = 1$. Since the

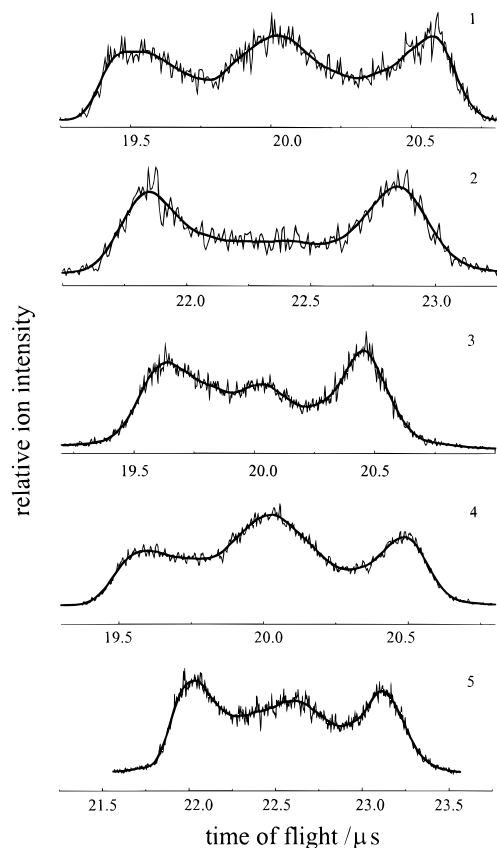


Figure 2. Acceleration time of flight profiles for two states in $v = 0$ and three states in $v = 1$ (cf. Table 1). The solid lines result from smoothing the raw data. Characteristic features in all profiles are maxima at the wings, caused by forward and backward flying particles in conjunction with ion fly-out. Some profiles exhibit more or less pronounced third maxima at the line center indicating a bimodal kinetic energy distribution.

parent molecule is efficiently cooled in the jet expansion, the angular momentum of the CO product must be generated in the dissociation process. Separated, Doppler broadened lines with a width significantly broader than the laser line width of 0.2 cm^{-1} for higher rotational states with $J'' \geq 30$ in the 0–0 band serve as an independent test for the correctness of the kinetic energy distributions obtained from the TOF profiles via line shape analysis.

The very intense ion signal for low rotational levels at the bandhead of the 0–0 band is well described by a Boltzmannian distribution of overlapping lines ($J'' = 0, 1, 2$) with a temperature parameter of 15 K. This part of the spectrum is not due to nascent CO products from the photolysis of phosgene but results from CO impurities cooled to 15 K in the supersonic expansion. Therefore, this part of the spectrum serves as a “thermometer” to determine the initial temperature of the phosgene parent molecule.

2. CO Time-of-Flight Profiles. Acceleration and drift TOF profiles that were observed at the marked positions of Figure 1 are shown in Figures 2 and 3. The drift profiles consist of a single peak with a low kinetic energy (large TOF) tail with the peak position shifted according to the variation of the total kinetic energy ϵ with the CO quantum state. All acceleration profiles exhibit two characteristic maxima, which are caused by forward and backward flying particles in conjunction with particles with high velocity components perpendicular to the spectrometer axis, flying out of the detector region. The presence of ion fly-out is proven by the lower ion intensities at the centers of the TOF profiles in comparison to the wings and

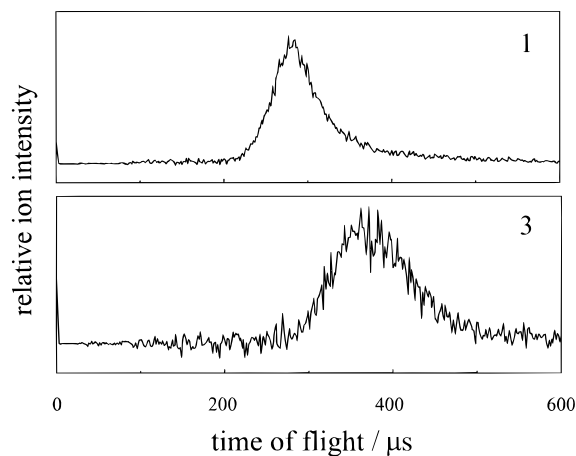


Figure 3. Typical drift time of flight profiles for $v = 0, J = 31(1)$ and $v = 1, J = 14(3)$. Drift profiles exhibit single TOF peaks followed by a tail at large TOF, corresponding to low kinetic energies. The peak position is determined by the internal energy of the observed CO quantum state.

implies the generation of fragment velocities higher than the ratio of t_0 , the center of the profile, and the detector radius r_D , which in our case ($t_0 = 20 \text{ μs}$, $r_D = 2 \text{ cm}$) amounts to 1000 m/s. The fragments missing due to fly-out are accounted for in the data analysis procedure, which has previously been outlined in detail.^{3,41}

The TOF profiles of Figure 2 have two additional features to be considered. First, for increasing rotational and vibrational excitation of the fragments a smaller width of the TOF profiles is found. This observation corresponds to a decreasing kinetic energy content for increasing internal energies of the fragments. This effect is also seen for the Doppler broadening, but it is small enough to not affect the accuracy of the determination of the rotational state population, which assumed a common width for all rotational levels. Second, some profiles have a third maximum at the center, which is equivalent to a bimodal kinetic energy distribution. After careful consideration of possible artifacts (collisions of the ionized CO with other particles or with the walls, simultaneous excitation of neighboring rotational levels, fragmentation of the ionized parent molecular ion, nonresonant ionization of CO, clustering of phosgene in the supersonic expansion), we were led to conclude that the third maxima do reflect the dynamics of the decay process. Each of the above hypotheses would result in different experimentally observable effects on the shape of the TOF profiles and can be investigated by changing the experimental parameters, as there are the stagnation pressure of phosgene prior to the expansion, laser intensity, and wavelength. However, for none of these parameters the expected variations of the shape of the TOF profile was observed. Moreover, it is not plausible why only some rotational levels should be affected in the present experiments, conducted under identical conditions for all rotational levels investigated. Thus, the corresponding bimodalities are real and will play an important role in the discussion of the decay dynamics.

We also observed drift and acceleration profiles in the 0–0 bandhead for $v'' = 0, J'' = 0$. The data evaluation is hindered by the very large signal resulting from jet-cooled CO, especially for the acceleration data, where all slow CO molecules create a signal at the detector. The corresponding profile looks qualitatively different, as has previously been discussed.² In contrast, the drift mode is blind for those particles, and correspondingly a weak signal was observed for CO with high kinetic and zero internal energy. In the analysis procedure this

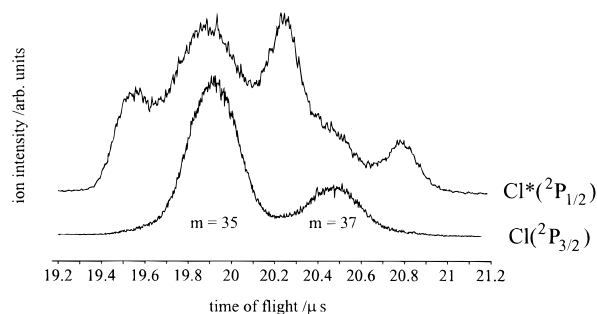


Figure 4. Velocity broadened mass peaks, obtained in the acceleration mode of the ^{35}Cl and ^{37}Cl isotopes, for both $\text{Cl}(^2P_{3/2})$ and $\text{Cl}^*(^2P_{1/2})$ spin-orbit states. The line shapes are qualitatively different: A higher kinetic energy release for $\text{Cl}^*(^2P_{1/2})$ causes the overlap of forward flying ^{37}Cl with backward flying ^{35}Cl .

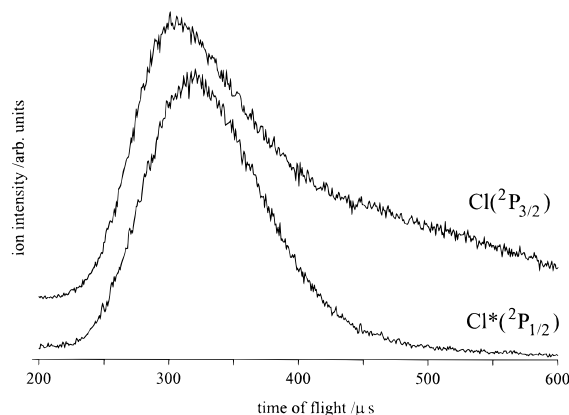


Figure 5. Drift TOF profiles for both $\text{Cl}(^2P_{3/2})$ and $\text{Cl}^*(^2P_{1/2})$ spin-orbit states. The peak for $\text{Cl}(^2P_{3/2})$ is shifted to shorter times due to the lack of internal excitation and a slightly shorter dissociation wavelength. The large portion of slow $\text{Cl}(^2P_{3/2})$, seen in Figure 4, is contained in the large TOF (low energy) tail in the upper curve.

part of the spectrum has not been considered due to the incompleteness of the data.

3. Cl Time-of-Flight Profiles. The TOF profiles of the $\text{Cl}(^2P_{3/2})$ and $\text{Cl}^*(^2P_{1/2})$ products obtained in drift and acceleration modes are shown in Figures 4 and 5. The profiles are normalized with respect to peak height and, thus, do not reflect the Cl^*/Cl branching ratio, which has been determined to be 0.18.³ The drift profile for ground state Cl in Figure 5 peaks at lower TOF (corresponding to a higher kinetic energy) than the drift profile of excited state Cl^* due to the lack of electronic excitation of the Cl atom and the slightly shorter dissociation wavelength but has a pronounced tail at low kinetic energies. The qualitatively different behavior is strikingly evident in the acceleration profiles of Figure 4, where the velocity broadened mass peaks for the simultaneously observed ^{35}Cl and ^{37}Cl isotopes in their natural 3:1 abundance are shown for both spin-orbit states. The effect causes the two isotopes of excited Cl^* to exhibit overlapping TOF profiles, while the two masses for ground state Cl are still clearly separated from one another. The overlap is due to identical TOF for backward flying $^{35}\text{Cl}^*$ and forward flying $^{37}\text{Cl}^*$, which have higher kinetic energies than their corresponding ground state isotopes.

In order to confirm that the observed effect is solely due to the spin-orbit state that is being monitored and not to the variation in dissociation energy, additional TOF profiles for Cl^* were recorded with the $2P_{1/2}^0$ state as resonant intermediate at a wavelength of 235.205 nm instead of the $2D_{3/2}^0$ state at 237.808 nm. Since the Cl^* profiles obtained for the different intermediate states are indistinguishable from one another, state selective energy partitioning is indeed taking place: ground state Cl atoms

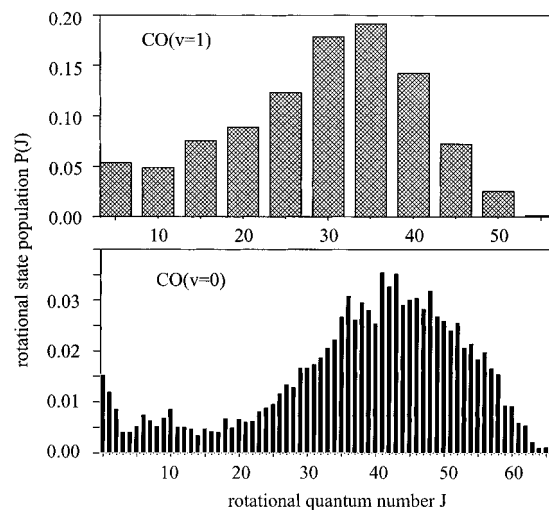


Figure 6. Rotational state populations of CO in $v = 0$ (lower panel) and $v = 1$ (upper panel) from the photodissociation of phosgene as analyzed from the spectra in Figure 1. The distributions are neither thermal nor statistical. Due to the rotational overlap for $v = 1$ intervals containing five rotational states, each have been evaluated rather than single rotational states.

are preferentially produced with low kinetic energies, while excited state Cl^* atoms are preferentially produced with large kinetic energies.

IV. Discussion

A. Rotational Population of the CO Fragments. Figure 6 shows the rotational populations of the $v'' = 0$ and $v'' = 1$ states as determined from the spectra shown in Figure 1. Each rotational line of the 0–0 band has been fitted by a Gaussian function with common width $\Delta\nu$. Thus, the amplitudes describe the intensities of the transitions, taking into account the $(2J''+1)$ -fold degeneracy.^{68,69} $\Delta\nu$ has been determined from the separated high J'' lines, assuming this width to be constant for all J'' , which in good approximation is the case. The use of Gaussian functions is justified since the TOF data yield broad kinetic energy distributions, which, although not Boltzmannian, give rise to almost Gaussian Doppler line shapes. The distribution for $v'' = 0$ peaks at $J'' = 43$ and can be characterized neither by a temperature parameter nor by statistical energy distribution. The mean rotational excitation is 3240 cm^{-1} , which again is proof of the dynamic generation of angular momentum in the dissociation process. For determining the rotational population of the 1–1 band the procedure was modified, because the rotational lines are not separated from each other and their width is unknown. In the analysis of the spectrum we considered the intensities of intervals containing five rotational levels each and compared the intensities of those intervals to each other. Using this approach we obtained the rotational population for $v'' = 1$, also shown in Figure 6, which is similar to the one for $v'' = 0$. The maximum is found around $J'' = 37$, and the mean rotational energy is 1650 cm^{-1} . This shift to lower energies amounts to 73% of the vibrational energy.

B. Fragment Kinetic Energy Distributions. The independence of the shapes of the TOF and the Doppler profiles of the polarization direction of the laser indicates an isotropic fragment distribution under the present experimental conditions. The data evaluation procedure for obtaining kinetic energy distributions from the combined acceleration and drift TOF profiles makes implicit use of the isotropic fragment distribution.^{2,41} In the absence of ion fly-out for the acceleration measurements, due to the linear relationship (18) between the measured quantity,

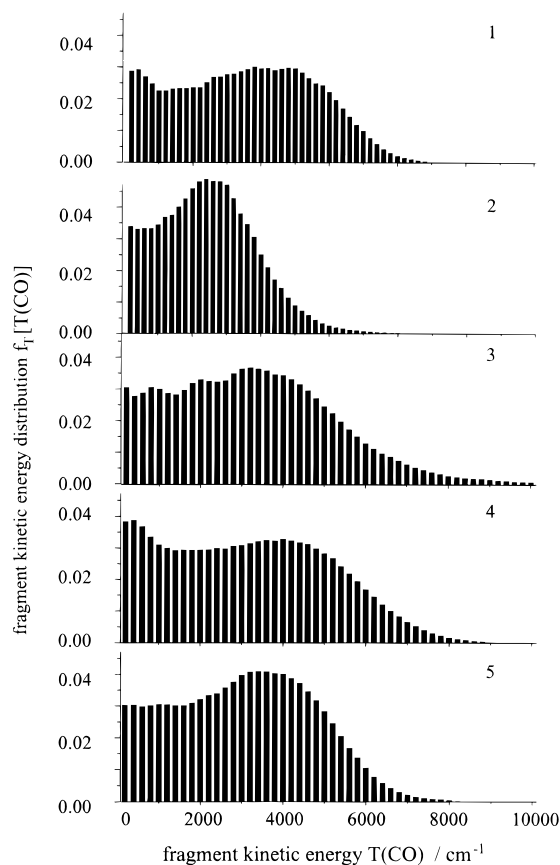


Figure 7. Complete kinetic energy distributions for all investigated states from the analysis of the combined acceleration and drift TOF data, as described in the text. The ordinate is scaled with respect to the abundance of CO molecules in kinetic energy intervals of 200 cm^{-1} width.

the flight time deviation Δt from the center of the TOF profile t_0 , and the velocity component v_x along the spectrometer axis, the TOF data evaluation procedure is identical to the evaluation procedure for Doppler profiles, with Δt replacing $\Delta \nu$, the Doppler shift, and t_0 replacing ν_0 , the line center. In particular, an isotropic single-valued velocity distribution yields a rectangular profile and a Boltzmannian distribution manifests itself in a Gaussian TOF profile. While for the given geometry no laboratory to center of mass transformation is required, ion fly-out must be accounted for, however, which can best be done by an iterative procedure as previously described.^{3,41} In contrast, for the drift measurements the laboratory to center of mass transformation is essential.

In short, the procedure followed here was to first convert the drift data to highly accurate velocity distributions which are characteristic of the high energy particles but lack information about slow particles. Second, the iteration procedure yielded complete velocity distributions from the acceleration data with a lower degree of accuracy, which subsequently were adjusted within the experimental error (mainly resulting from the finite duration of the laser pulse) to match the drift data. Finally, the accurate and complete velocity distributions were converted to the desired kinetic energy distributions. Following this procedure, the kinetic energy distributions of Figure 7 were obtained. The respective CO quantum states are listed in Table 1.

The transformation of the TOF profiles in kinetic energy distributions leads to a much higher density of data points for low energies as compared to higher energies. In order to avoid a higher weight of the low energy amplitudes in the fit procedure, we calculated mean values for a standard size interval of fragment kinetic energy, before actually performing the fits.

The width of these intervals has been chosen to be 200 cm^{-1} , which is small enough to keep sufficient data points for the fit procedure and represents approximately the kinetic energy resolution of the apparatus in the relevant energy range.

The data extracted from the fragment energy distribution are compiled in Table 1. For each investigated state the mean kinetic energy \bar{T} has been determined. High internal CO excitation coincides plausibly with low CO kinetic energy contents. Correspondingly a broad range for the respective mean kinetic energies of the Cl partner fragments must be observed. These were calculated from the energy amount by which the total available energy exceeds the sum of the CO energies in all degrees of freedom, based on the assumption that two ground state chlorine atoms with equal mean kinetic energies will be produced.

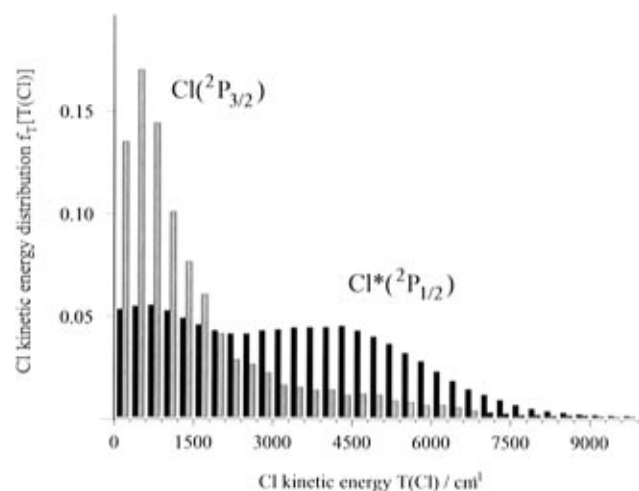
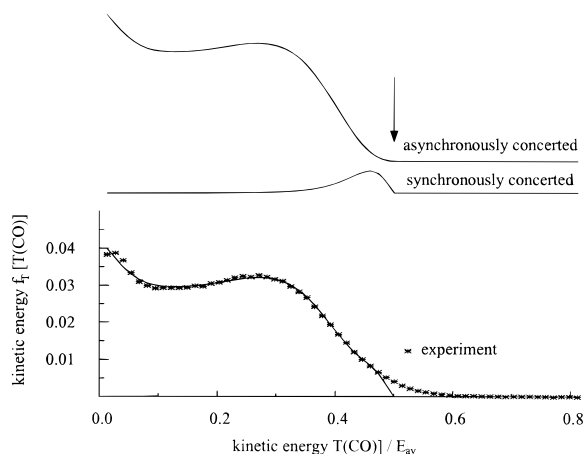
The state specific kinetic energy distributions of the Cl products, obtained in the same way as for the CO fragments, are shown in Figure 8. The state specific mean kinetic energies are extracted to be $\bar{T}(\text{Cl}) = 1520 \text{ cm}^{-1}$ and $\bar{T}(\text{Cl}^*) = 3170 \text{ cm}^{-1}$, respectively, with an upper limit of 5% for the experimental error, estimated from the drift mode response function. A bimodal kinetic energy distribution, which is obvious for the excited state Cl^* fragment, also is appropriate to describe the ground state Cl kinetic energy distribution, which at first glance consists of a single peak with a high energy tail attached to it. Each of the translational spectra can be fitted by a sum of two Gaussian functions, one of which is centered around 350 cm^{-1} (low energy component), while the other one (high energy component) is centered around 3850 cm^{-1} for ground state Cl and around 4000 cm^{-1} for excited state Cl^* . The fit parameters are listed in Table 2.

C. CO Fragment Kinematic Analysis. For each one of the kinetic energy distributions of the CO fragments individual fits were performed for the parameter values that characterize the respective decay channels. The agreement with the experimentally derived distributions considering one pure mechanism only was in general poor. Therefore, competing mechanisms must operate. The competition between different channels was accounted for by using eq 14, fitting the respective parameters ($P_{i,0}$ and ΔP_i) and amplitudes A^i . In Figure 9 the top panels show the contributions of each decay channel to the decay process, while the bottom panel matches the experimental data (asterisks) with the fit result that is obtained by summing up the individual contributions according to the values of the corresponding amplitudes A^i . The agreement between the calculated and the experimental data is very good qualitatively as well as quantitatively, if competing pathways are considered. A minor discrepancy remains in the high energy part of the spectrum and is due to the resolution of our apparatus and to the neglect of the possible insignificant contribution of a molecular channel.

The best results were obtained from a complex dissociation process, where an asynchronously concerted mechanism dominates the decay, competing with a minor synchronously concerted channel. The contribution of the asynchronously concerted channel accounts for more than 80% of all decay processes, with a standard deviation of 20%. No tendency for a change of this value is found for changes in the internal excitation of the CO fragments. CO is mainly scattered in forward direction ($\theta = 180^\circ$) with a very broad distribution of the decay angle. The intermediate COCl particle, which exists only in the very short period between the first and the second C—Cl bond cleavages, carries on the average 11% more of the total available energy E_{av} as internal excitation than is eventually found as internal energy of the CO product. The kinetic energy

TABLE 1: Characteristic Data Describing the Kinetic Energy Distributions of the CO Fragments in the COCl₂ Dissociation

profile	<i>J</i>	<i>ν</i>	<i>E</i> _{rot} (CO)	<i>E</i> _{vib} (CO)	\bar{T} (CO)	\bar{T} (Cl)	\bar{T}_{tot}	<i>f</i> _{rot}	<i>f</i> _{vib}	<i>f</i> _{kin}
1	31	0	1910	0	3450	4710	12 870	0.13	0.00	0.87
2	61	0	7300	0	2350	2565	7 480	0.49	0.00	0.51
3	14	1	420	2170	3390	4400	12 190	0.03	0.15	0.82
4	34	1	2370	2170	3100	3570	10 240	0.16	0.15	0.69
5	44	1	3930	2170	2960	2860	8 680	0.27	0.15	0.58

**Figure 8.** Complete kinetic energy distributions for both Cl(²P_{3/2}) and Cl*(²P_{1/2}) spin-orbit states from the analysis of the combined acceleration and drift TOF data. Details of the respective high and low energy components of the bimodal distributions are listed in Table 2.**Figure 9.** Fit of the decay models (solid lines) to the experimentally observed data (asterisks) for profile 3 (*ν* = 1, *J* = 14). The contributions of the synchronously and asynchronously concerted mechanisms are shown separately in the upper part. The sum of both is shown together with the experimental data in the bottom part. The arrow marks the limiting energy that separates the three body from the molecular decay channel. The contribution of the molecular channel is insignificant.**TABLE 2: Characteristic Data Describing the Kinetic Energy Distributions of the Cl Fragments in the COCl₂ Dissociation**

	Cl*(slow)	Cl*(fast)	Cl(slow)	Cl(fast)	Cl*	Cl
<i>A</i>	4%	11%	71%	14%	15%	85%
<i>T</i> ₀ /cm ⁻¹	350	4000	350	3850		
ΔT /cm ⁻¹	1600	2600	1380	2500		
\bar{T}_{rot} /cm ⁻¹	1040	4070	920	3910	3190	1430
<i>T</i> _{exp} /cm ⁻¹					3170	1520

release in the second step is therefore small and does not significantly influence the kinetic energies of the final fragments. Due to the forward scattering the CO increases its kinetic energy by a small amount, whereas the kinetic energy of the chlorine atom from the second decay step is accordingly decreased.

TABLE 3: Results of the Fit Procedure for the CO Fragments, Based on the Kinematic Evaluation Scheme

	profile(<i>ν</i> , <i>J</i>)					mean
	1(0,31)	2(0,61)	3(1,14)	4(1,34)	5(1,44)	
<i>E</i> (CO)	0.13	0.49	0.20	0.31	0.41	
<i>A</i> ^{conc}	95%	62%	81%	94%	89%	84%
<i>A</i> ^{syn}	5%	35%	17%	4%	8%	14%
<i>A</i> ^{mol}	0%	<3%	<2%	<2%	<3%	<2%
<i>E</i> _{COCl,0}	0.27	0.56	0.22	0.47	0.56	
ΔE_{COCl}	0.13	0.06	0.10	0.15	0.13	0.12
<i>E</i> _{COCl,0} − <i>E</i> (CO)	0.14	0.07	0.02	0.16	0.15	0.11
θ_0	190°	184°	182°	182°	187°	185°
$\Delta\theta$	190°	183°	231°	215°	160°	196°
α_0	98°	111°	112°	67°	68°	103°
$\Delta\alpha$	29°	37°	30°	32°	34°	34°

Owing to its large mass, the velocity of the COCl intermediate is always small, too, so that a large fraction of slow chlorine atoms is expected from the CO kinetic energy data. However, because of the broad decay angle distribution the opposite case, forward scattered chlorine atoms and backward scattered CO molecules, contributes to a nonnegligible extent, giving rise to the low energy maxima in the CO fragment kinetic energy distributions which in turn are responsible for the previously discussed third maxima observed in the acceleration TOF data.

The parameter distributions for the asynchronously concerted decay channel are listed in Table 3. Although every possible decay angle is realized in the phosgene dissociation, there exist different weights for every decay angle. Accordingly the independence criterion is in general not fulfilled, although some COCl intermediate particles must have longer lifetimes than their mean rotational periods τ_{rot} .

Therefore it is obvious that the lifetime of the COCl intermediate must be of the order of its mean rotational period or less, since otherwise the decay angle θ would be equally distributed and the process would be purely sequential. Thus, an upper limit for the COCl lifetime is obtained from comparison with its rotational period. Since there is no information available on the angular momentum of the COCl radical or its geometry, we rather crudely approximated a value of $\tau_{\text{COCl}} = 50$ ps for low rotational excitation (*J* = 1) and a linear geometry. This value is based on an estimated moment of inertia of 8×10^{-41} kg·m². Taking into account the nonplanar conformation of phosgene in the excited ¹A₂ state, the small rotational constants of COCl and COCl₂, and the high rotational excitation of the CO fragments, the actual angular momenta should be much higher and a lifetime τ_{COCl} in the order of 1 ps seems to be a more realistic value.

While the main features of the kinetic energy distributions are well reproduced by the asynchronously concerted mechanism, for high kinetic energies just below the limiting energy to the molecular regime, a satisfactory agreement is not achieved. This energy range can much better be described by contributions from the synchronously concerted mechanism. The excitation of Cl−C−Cl bending easily closes the gap between the calculated distribution on the basis of a pure asynchronously concerted mechanism and the experimental data. The reason is that, due to the projection of the chlorine atom velocities on the axis of motion of the CO fragment, large changes of the

(small) bond angle correspond to only minor changes of the (high) CO fragment recoil velocities.

The participation of the synchronously concerted channel is 14% on the average, with a standard deviation of 12%. The exact values are listed in Table 3. The mean bond angle of the excited phosgene molecule at the decay time is 103° . This value is close to the 111° Cl–C–Cl bond angle of the excited phosgene, which is exactly the same as the value for the ground state.¹⁹ This is a common feature for this class of molecule, which is also known for formaldehyde (H_2CO)⁷⁰ and thiophosgene (CSCl_2).⁷¹ The width of the bond angle distribution is 34° on average and represents a relevant excitation of the ν_3 Cl–C–Cl bending mode. We did not attempt to quantitatively determine this excitation, since the potential energy surface for this mode is unknown and the harmonic oscillator approximation is inappropriate for this large excitation. That the excitation is significant indeed can be seen from the comparison with the zero point amplitude, which we estimated to be 5° , approximating the bending vibration by a linear oscillation of the two Cl atoms with the force constant of the bending mode.

If instead of two Cl atoms, a Cl_2 molecule is produced, the additional bond energy (diminished by any excitation of the Cl_2 molecule) increases the value of the available energy E_{av} . Thus, there exists a limiting kinetic energy $T_l(E(\text{CO}))$ for every CO state, sharply dividing the molecular regime ($\text{COCl}_2 + h\nu \rightarrow \text{CO} + \text{Cl}_2$) from the three body regime ($\text{COCl}_2 + h\nu \rightarrow \text{CO} + 2\text{Cl}$) in the translational energy spectra:

$$T_l(E(\text{CO})) = \frac{m_{\text{Cl}_2}}{m_{\text{COCl}_2}}(E_{\text{av}} - E(\text{CO})) \quad (19)$$

This limiting energy depends on the internal excitation of the observed CO fragment and is marked in Figure 9 by an arrow. Kinetic energies higher than the limiting energy, i.e., on the right-hand side of the arrow, correspond to the molecular channel; kinetic energies lower than the limiting energy, i.e., on the left-hand side of the arrow, belong to a three body channel. In no case the integration of the experimental data in the corresponding high energy parts of the observed kinetic energy distributions yielded a contribution of more than 3% for the molecular decay. The detailed data can be found in Table 3.

It is likely, however, that the molecular channel does not contribute at all to the overall decay and that the amplitudes merely represent upper limits: First, the energetic range of the molecular regime, where we observed nonzero values, is very narrow compared to the dissociation energy of the chlorine molecule: $D_0(\text{Cl}_2) = 20\,000\text{ cm}^{-1}$. If the participation of the molecular channel were real, exclusively very highly internally excited chlorine molecules would be produced, with the internal excitation close to the dissociation limit, a scenario which is very unlikely. Second, the resolution of ca. 5% of our apparatus has not explicitly been taken into account by a deconvolution procedure for the experimental data. A forward convolution of the calculated kinetic energy distributions leads to kinetic energy values above the limiting energy, which is exactly the observed effect, without implying the generation of a chlorine molecule.

D. Cl Fragment Kinematic Analysis. A similar procedure as was performed for the CO fragments is not well suited in order to analyze the Cl atom kinetic energy distribution. For CO numerous quantum states could selectively be observed where the atomic partner fragment only possesses two energetically accessible quantum states (which are only separated in energy by 881 cm^{-1}). For Cl the situation is reversed: Only

TABLE 4: Interdependence of Kinetic Energies of Both CO and Cl Fragments for the Asynchronously and the Synchronously Concerted Mechanisms

	profile(ν, J)					
	1(0,31)	2(0,61)	3(1,14)	4(1,34)	5(1,44)	mean
Asynchronously Concerted Mechanism						
$E(\text{CO})$	0.13	0.49	0.20	0.31	0.41	
$\bar{T}^{\text{conc}}(\text{CO})$	0.24	0.13	0.19	0.20	0.19	0.19
$\bar{T}^{\text{conc}}(\text{Cl}^1)$	0.49	0.26	0.45	0.38	0.32	0.38
$\bar{T}^{\text{conc}}(\text{Cl}^2)$	0.14	0.12	0.16	0.11	0.08	0.12
Synchronously Concerted Mechanism						
$E(\text{CO})$	0.13	0.49	0.20	0.31	0.41	
$\bar{T}^{\text{syn}}(\text{CO})$	0.44	0.22	0.36	0.43	0.36	0.36
$\bar{T}^{\text{syn}}(\text{Cl})$	0.21	0.14	0.22	0.13	0.11	0.16

two observable Cl quantum states correlate with a large number of energetically accessible CO quantum states. Therefore, every experimentally observed Cl atom kinetic energy distribution is a superposition of many different translational spectra with CO partner fragments in different quantum states, and separating the individual contributions is not feasible. Therefore, the statistic evaluation procedure is more appropriate in this case.

Nevertheless, some qualitative results can be obtained from comparing the experimentally observed Cl atom translational energy spectra of Figure 8 with conclusions drawn from the discussion of the CO kinetic energy distributions presented in the previous section. With the knowledge of the parameter distributions for each decay mechanism, a mechanism specific determination of the mean kinetic energies of the CO molecule is possible. Having experimentally observed the internal CO energy, the corresponding mean kinetic energies of the chlorine atoms can be obtained in a mechanism specific manner from the experimental data of the CO fragments. The energies obtained via this approach are compiled in Table 4, where the basis for the calculation was the generation of two ground state chlorine atoms. Thus, no additional internal energy, apart from the known value for CO, had to be considered, neglecting the small production of electronically excited $\text{Cl}^*(^2\text{P}_{1/2})$ atoms in the near-UV photodissociation of COCl_2 .^{3,4}

It can be seen from the data in Table 4 that the asynchronously concerted mechanism produces one fast and one slow chlorine atom at a time, while the synchronously concerted decay produces two slow atoms. The fast atom, resulting from the first bond cleavage in the asynchronously concerted decay, carries almost all kinetic energy that is released in the dissociation process. Its velocity therefore depends strongly on the internal excitation of the CO molecule. This dependence is indeed seen in Table 4, as is the much weaker dependence of the velocity of the second chlorine atom on the CO internal energy. The generation of two slow chlorine atoms by the synchronously concerted mechanism is also a consequence of associating the fastest CO molecules with this mechanism.

The kinetic energy of the chlorine fragments is therefore contributed to by three qualitatively different channels: (a) the first bond cleavage of the asynchronously concerted mechanism, (b) the second bond cleavage of the asynchronously concerted mechanism, and (c) the synchronously concerted mechanism. Channel (a) induces significantly larger kinetic energies in the corresponding chlorine fragment than the other two channels and should therefore be experimentally distinguishable from those. The energies of the products from channels (b) and (c) are very similar, however, and cannot be expected to be experimentally resolved. From these arguments we expect from the CO experimental data a bimodal kinetic energy distribution for the chlorine fragments, where we estimate for the centers a value of 13% of the total available energy for the slow

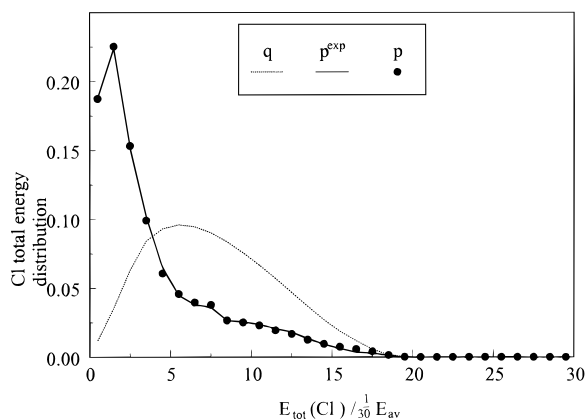


Figure 10. One dimensional total energy distributions for the Cl atom. The dots mark experimental data; the broken line shows a statistic distribution according to a prior distribution; the solid line is the distribution obtained from the modified joint probability matrix P .

component and a value of 38% for the fast component. These values are derived from the mean kinetic energies of Table 4 after weighting with the contributions of the two considered mechanisms. Consequently, the intensity ratio of the slow to the fast component is given by $(A^{\text{conc}} + 2A^{\text{syn}})/A^{\text{conc}} = 1.3$.

The experimentally observed kinetic energy distributions in section B3 show a satisfactory agreement with the predictions made above, for they do exhibit the bimodality, but quantitatively a discrepancy remains. The observed intensity ratio for slow and fast Cl atoms is larger by more than a factor of 2 (3 instead of 1.3), and also the mean kinetic energy values of 7% and 29% (instead of 13% and 38%) of the total available energy are different and do not lie within the experimental error of the CO data analysis.

This quantitative discrepancy can be explained by the generation of highly vibrationally excited CO molecules ($\nu_{\text{CO}} \geq 2$), which are not experimentally observable with the detection scheme employed in our experiments due to the predissociation of the intermediate resonant $B^1\Sigma^+$ state. The main argument favoring this explanation is the smaller values for the chlorine atom kinetic energies as compared to the expectations. It must be remembered in this context that a higher internal excitation of the CO molecule takes the energy mainly from the fast chlorine atom and, to a lesser degree only, from the slow atom. The difference in the intensity ratios suggests a higher contribution of the synchronously concerted channel for highly vibrationally excited CO fragments, favoring the generation of only slow Cl atoms. Thus, information about the spectroscopically inaccessible CO states can be obtained from analyzing the experimental observations of the Cl atoms. Owing to the large number of CO quantum states correlating with only two energetically accessible Cl quantum states, the statistic analysis procedure is a more powerful tool for interpreting the Cl kinetic energy distributions than the kinematic procedure.

E. Statistical Analysis. The number of elements in the joint probability matrix $P(jkl)$ depends on the desired accuracy. For the phosgene dissociation to be described with a resolution of 3% of the available energy, E_{av} (13 800 cm^{-1} at 235.3 nm) was divided into 30 intervals of approximately 450 cm^{-1} width. From conservation of energy there are only 465 elements (jkl) in this matrix possibly different from zero.

The prior probability matrix peaks at a total energy $E_{\text{tot}}(\text{CO})$ of 60% E_{av} , while the maximum probability for Cl atoms is obtained for 20% E_{av} . The corresponding one-dimensional prior distribution $q(\text{Cl})$ for a single Cl atom is shown in Figure 10 along with the experimentally observed distribution $p^{\text{exp}}(\text{Cl})$ (which is weight averaged over the spin-orbit states). Obvi-

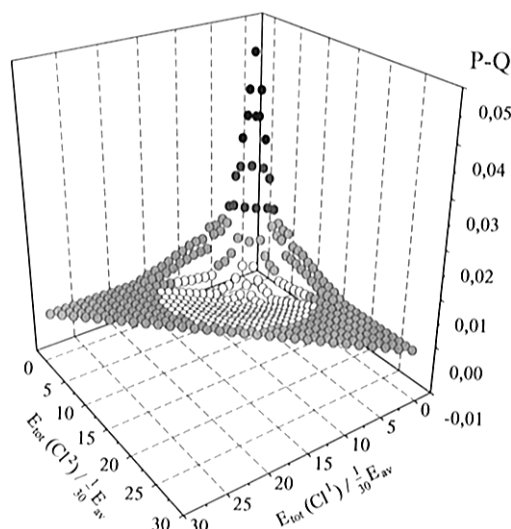


Figure 11. Difference matrix, obtained from subtracting the prior joint probability matrix Q from the modified matrix P . The probability increases strongly for the coincident generation of two slow chlorine atoms, decreases for the simultaneous generation of two fast atoms, and increases moderately for the coincident production of one slow and one fast atom.

ously, the prior distribution q does not satisfactorily describe the phosgene dissociation as a statistic process.

The modification of the prior probability matrix $Q(jkl)$ in order to obtain a joint probability matrix $P(jkl)$ which is in agreement with the experimental data led to a difference matrix $P(jkl) - Q(jkl)$, which is shown in Figure 11 for the total energies $E_{\text{tot}}(\text{Cl}^1)$ and $E_{\text{tot}}(\text{Cl}^2)$ of the two chlorine fragments (Cl^1 and Cl^2 denote the first and the second chlorine atom of the same decay process, respectively). The diagram shows the minimum deviation from statistical behavior that is capable of reproducing the experimental results. One sees a dramatic probability increase for the production of two Cl atoms with low kinetic energies (near the origin), a decrease for the simultaneous production of two fast atoms, and a moderate increase for the coincident generation of one slow and one fast atom. The excellent agreement of the modified probability matrix $P(jkl)$ with the experimental data can also be seen in Figure 10, where the one-dimensional total kinetic energy distribution $p(\text{Cl})$, calculated from the modified matrix, is given by the filled dots along the experimentally observed distribution $p^{\text{exp}}(\text{Cl})$ (solid line).

The corresponding angular distribution for χ , the angle of the direction of motion of the COCl center of mass, induced by the first bond cleavage, with the direction of motion of the Cl atom from the second bond cleavage, also shows a pronounced nonstatistical behavior (cf. Figure 12). There is a probability increase for $\cos \chi = -1$, or $\chi = -\pi$, meaning a preferentially parallel motion of the two chlorine atoms. This is in accordance with the forward scattering of the CO molecule, which was deduced in the previous section. Moreover, it is proof of the concerted character of the decay process, since for a sequential, nonconcerted mechanism no one angle should be preferred over others.

With respect to synchronicity, the probability increase for simultaneously producing one slow and one fast Cl atom is evidence of a significant contribution of the asynchronously concerted mechanism. The coincidently generated slow Cl atoms could be as well generated in a synchronously as in an asynchronously concerted process, but taking into account the angular information, i.e., the preference for backward scattering of the second Cl atom, the asynchronously concerted mechanism

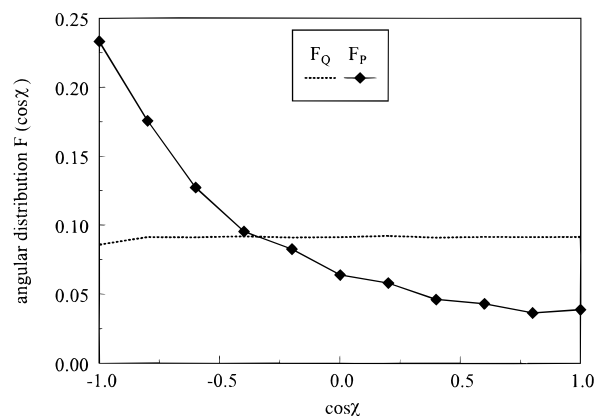


Figure 12. Distribution of the angle χ , describing the spatial fragment distribution, respectively the concertedness of the reaction. The broken line describes a completely statistic (sequential) decay, where the probability for all angular values is equal. The data (dots and solid line) obtained from the modified joint probability matrix P differ strongly from that prior angular distribution, indicating a concerted mechanism. The distribution peaks at $\chi = -\pi$, which means that both chlorine atoms move preferentially in the same direction, whereas the CO molecule will mainly be scattered in the forward direction with respect to the direction of motion of the COCl intermediate in the lab system.

must be responsible for this portion of fragments as well. Only those parts of the probability matrix that are unchanged or diminished, when calculating P from Q , can be associated with a synchronous decay, which consequently is concluded to be of minor importance compared to the principal asynchronously concerted channel.

The projection of P onto the total energy axis of the CO fragments yields a distribution with significantly higher energy as compared to the prior distribution, peaking at 80% E_{av} . Although the evaluation procedure does not allow to distinguish between the different degrees of freedom of the CO molecules, from the observed rotational populations of the CO fragments in $v'' = 0, 1$ and the low mean kinetic energies of the Cl fragments, taking into account the conservation of linear and angular momenta, a significant vibrational excitation (up to $v'' \geq 3$) is expected, which should be caused by a strong vibrational excitation of the phosgene molecule, due to a strong gradient of the excited potential energy surface with respect to the out-of-plane coordinate ν_4 and the large difference between the CO bond lengths in the fragment and in the parent molecule.

V. Concluding Remarks

The three body decay of phosgene has been analyzed by two conceptually different analysis procedures, and a clear picture of the dissociation process has been obtained. One approach is based on kinematic analysis under strict application of conservation laws. The definition of decay mechanisms with introduction of physically meaningful parameters and the consequent consideration of parameter distributions lets us gain detailed insight into the dissociation dynamics without requiring wave packet evolution calculations or the knowledge of the involved potential energy surface topologies. This approach is particularly well suited for molecules the size of phosgene, being beyond today's capabilities to perform quantum mechanical calculations, being simple enough, however, not to exhibit too many product degrees of freedom that would finally reduce the significance of the results of the kinematic method. In any case, in order to obtain meaningful data, at least one dissociation product has to be experimentally well-characterized, meaning the knowledge of product state and kinetic energy distributions,

preferably as a joint distribution matrix. The second approach is based on a statistical procedure, where probabilities of coincidentally generating sets of quantum states of all particles are evaluated and, aiming at maximum entropy in the corresponding joint probability matrix, are modified in order to reproduce the experimental results when projected onto the corresponding observable quantities. This approach is appropriate, when the experimental data are scarce or if partner products in a large variety of quantum numbers are produced. Therefore, the phosgene molecule is ideally suited to compare the two methods: On observing the kinetic energy distribution of the carbon monoxide molecule, one faces the first situation, and the kinematic analysis should be chosen, while on observing the chlorine fragment, the conditions of the second situation apply, and the statistic approach is to be chosen.

Considering the different concepts underlying the analysis procedures, the results obtained in both cases match remarkably well. They can be summarized as follows: No significant contribution of a molecular channel, producing chlorine molecules, was found. Likewise, the generation of a stable chloroformyl radical had been ruled out in previous studies, so that every dissociation process upon irradiation around 230 nm yields three fragments: two chlorine atoms and a carbon monoxide molecule. For this three body decay, the asynchronously concerted mechanism is the dominant dissociation channel, accounting for over 80% of the products. The chlorine fragments move preferentially in the same direction, resulting in forward scattering of the carbon monoxide. A less abundant decay channel is the synchronous mechanism, in which the two bonds cleave in unison and which accounts for the remaining products. The geometry of the decaying parent resembles the ground state equilibrium geometry with significant excitations of the COCl₂ bending modes. For both mechanisms the CO fragments are generated with high internal excitation.

Acknowledgment. We thank Prof. F. J. Comes and Prof. E. A. Reinsch for stimulating discussions. Financial support of the Deutsche Forschungsgemeinschaft and the Fonds der Chemischen Industrie is gratefully acknowledged.

References and Notes

- (1) Dewar, M. J. S. *J. Am. Chem. Soc.* **1984**, *106*, 209.
- (2) Maul, C.; Gericke, K.-H. *Int. Rev. Phys. Chem.* **1997**, *16*, 1.
- (3) Maul, C.; Haas, T.; Gericke, K.-H.; Comes, F. J. *J. Chem. Phys.* **1995**, *102*, 3238.
- (4) Chichinin, A. I. *Chem. Phys. Lett.* **1993**, *209*, 459.
- (5) Helas, G.; Wilson, S. R. *Atm. Environ.* **1992**, *26A*, 2975.
- (6) Wilson, S. R.; Crutzen, P. J.; Schuster, G.; Griffith, D. W. T.; Helas, G. *Nature* **1988**, *334*, 689.
- (7) Kindler, T. P.; Chameides, W. L.; Wine, P. H.; Cunnold, D. M.; Alyea, F. N.; Frank, J. A. *J. Geophys. Res.* **1995**, *100*, 1235.
- (8) Robinson, G. W. *J. Chem. Phys.* **1953**, *21*, 1741.
- (9) Herzberg, G. *Molecular Spectra and Molecular Structure III, Electronic Spectra and Electronic Structure of Polyatomic Molecules*; Van Nostrand Reinhold: New York, 1966.
- (10) Ananthakrishnan, R. *Proc. Ind. Acad. Sci.* **1937**, *5A*, 285.
- (11) Bailey, C. R.; Hale, J. B. *Philos. Mag.* **1938**, *25*, 98.
- (12) Nielsen, A. H.; Burke, T. G.; Waltz, P. J. H.; Jones, E. A. *J. Chem. Phys.* **1952**, *20*, 596.
- (13) Catalano, E.; Pitzer, K. S. *J. Am. Chem. Soc.* **1958**, *80*, 1054.
- (14) Overend, J.; Evans, J. C. *Trans. Faraday Soc.* **1959**, *55*, 1817.
- (15) Schneider, B.; Stoker, J. *Coll. Czech. Chem. Commun.* **1961**, *27*, 121.
- (16) Henri, V.; Howell, O. R. *Proc. R. Soc.* **1930**, *A128*, 178.
- (17) LaPaglia, S. R.; Duncan, A. B. F. *J. Chem. Phys.* **1961**, *34*, 125.
- (18) Giddings, L. E.; Innes, K. K. *J. Mol. Spectrosc.* **1963**, *8*, 328.
- (19) Moule, D. C.; Foo, P. D. *J. Chem. Phys.* **1971**, *55*, 1262.
- (20) Klee, S., private communication.
- (21) Gillotay, D.; Simon, P. C.; Dierckx, L. *Aeronomica A* **1993**, 368, 1.
- (22) Jäger, M.; Heydtmann, H.; Zetzsch, C. *Chem. Phys. Lett.* **1996**, *263*, 817.

- (23) Reinsch, E. A., private communication.
- (24) Heicklen, J. J. *J. Am. Chem. Soc.* **1965**, 87, 444.
- (25) Wijnen, M. H. J. *J. Am. Chem. Soc.* **1961**, 83, 3014.
- (26) Okabe, H. *J. Chem. Phys.* **1977**, 66, 2058.
- (27) Francisco, J. S.; Li, Z. *J. Phys. Chem.* **1989**, 93, 8118.
- (28) North, S. W.; Blank, D. A.; Gezelter, J. D.; Longfellow, C. A.; Lee, Y. T. *J. Chem. Phys.* **1995**, 102, 4447.
- (29) Trentelman, K. A.; Kable, S. H.; Moss, D. B.; Houston, P. L. *J. Chem. Phys.* **1989**, 91, 7498.
- (30) Kim, S. K.; Pedersen, S.; Zewail, A. H. *J. Chem. Phys.* **1995**, 103, 477.
- (31) North, S. W.; Blank, D. A.; Lee, Y. T. *Chem. Phys. Lett.* **1994**, 224, 38.
- (32) Deshmukh, S.; Hess, W. P. *J. Chem. Phys.* **1994**, 100, 6429.
- (33) Deshmukh, S.; Myers, J. D.; Xantheas, S. S.; Hess, W. P. *J. Phys. Chem.* **1994**, 98, 12535.
- (34) Lane, I. C.; Meehan, R.; Powis, I. *J. Phys. Chem.* **1995**, 99, 12371.
- (35) Kroger, P. M.; Riley, S. J. *J. Chem. Phys.* **1977**, 67, 4483.
- (36) Baum, G.; Effenhauser, C. S.; Felder, P.; Huber, J. R. *J. Phys. Chem.* **1992**, 96, 756.
- (37) Wang, H.; Chen, X.; Weiner, B. R. *J. Phys. Chem.* **1993**, 97, 12260.
- (38) Kawasaki, M.; Kasatani, K.; Sato, H.; Shinohara, H.; Nishi, N.; Ohtoshi, H.; Tanaka, I. *Chem. Phys.* **1984**, 91, 285.
- (39) Chen, X.; Wang, H.; Weiner, B. R.; Hawley, M.; Nelson, H. H. *J. Phys. Chem.* **1993**, 97, 12269.
- (40) Ahmed, M.; Blunt, D.; Chen, D.; Suits, A. G. *J. Chem. Phys.* **1997**, 106, 7617.
- (41) Maul, C. *Konkurrierende Dynamik beim Dreikörperzerfall von Molekülen*; Wissenschafts-Verlag Dr. Maraun, Frankfurt, Germany, 1995.
- (42) Haas, T. *Charakterisierung naszenter Photofragmente zur Aufklärung der Zerfallsdynamik von Stickstoffwasserstoffsäure und Phosgen*; Wissenschafts-Verlag Dr. Maraun, Frankfurt, Germany, 1995.
- (43) Strauss, C. E. M.; Houston, P. L. *J. Phys. Chem.* **1990**, 94, 8751.
- (44) Levine, R. D. *Annu. Rev. Phys. Chem.* **1978**, 29, 59.
- (45) Levine, R. D. *Adv. Chem. Phys.* **1981**, 239, 41.
- (46) Bernstein, R. B.; Levine, R. D. *Adv. At. Mol. Phys.* **1975**, 11, 215.
- (47) Haas, T.; Maul, C.; Gericke, K.-H.; Comes, F. J. *Chem. Phys. Lett.* **1993**, 202, 108.
- (48) Krupenie, P. H. *The Band Spectrum of Carbon Monoxide*, National Bureau of Standards 5; USGPO, Washington, 1966.
- (49) Loge, G. W.; Tiee, J. J.; Wampler, F. B. *J. Chem. Phys.* **1983**, 79, 196.
- (50) Arepalli, S.; Presser, N.; Robie, D.; Gordon, R. *Chem. Phys. Lett.* **1985**, 118, 88.
- (51) Huber, G.; Herzberg, G. *Molecular Spectra and Molecular Structure IV, Constants of Diatomic Molecules*; Van Nostrand Reinhold: New York, 1979.
- (52) Okabe, H. *Photochemistry of Small Molecules*; Wiley: New York, 1978.
- (53) Clear, R. D.; Riley, S. J.; Wilson, K. R. *J. Chem. Phys.* **1975**, 63, 1340.
- (54) Huebert, B. J.; Martin, R. M. *J. Phys. Chem.* **1968**, 72, 3046.
- (55) Mulliken, R. S. *Phys. Rev.* **1937**, 51, 310.
- (56) Herzberg, G. *Molecular Spectra and Molecular Structure I, Spectra of Diatomic Molecules*; Van Nostrand: Princeton, NJ, 1950.
- (57) Gibson, G. E.; Bayliss, N. S. *Phys. Rev.* **1933**, 44, 188.
- (58) Turner, L. A. *Phys. Rev.* **1926**, 27, 397.
- (59) Radziński, L. J.; Kaufman, V. J. *Opt. Soc. Am.* **1969**, 59, 424.
- (60) Matsumi, Y.; Tonokura, K.; Kawasaki, M. *J. Chem. Phys.* **1992**, 97, 1065.
- (61) LeRoy, R. J. *Can. J. Phys.* **1974**, 52, 246.
- (62) Li, L.; Lipert, R. J.; Lobue, J.; Chupka, W. A.; Colson, S. D. *Chem. Phys. Lett.* **1988**, 151, 335.
- (63) Tonokura, K.; Matsumi, Y.; Kawasaki, M. *J. Chem. Phys.* **1991**, 95, 5065.
- (64) Bashkin S.; Stoner, J. O. *Atomic Energy Levels and Grottrian Diagrams I*; North Holland: Amsterdam, Oxford, 1975.
- (65) Moore, C. E. *Atomic Energy Levels*; Circular 467, National Bureau of Standards, 1949.
- (66) Bashkin S.; Stoner, J. O. *Atomic Energy Levels and Grottrian Diagrams II*; North Holland: Amsterdam, New York, Oxford, 1978.
- (67) Halpern, J. B.; Zacharias, H.; Wallenstein, R. *J. Mol. Spectrosc.* **1980**, 79, 1.
- (68) Bray, R. G.; Hochstrasser, R. M. *Mol. Phys.* **1976**, 31, 1199.
- (69) Spiglanin, T. A.; Perry, R. A.; Chandler, D. W. *Chem. Phys. Lett.* **1987**, 141, 428.
- (70) Jones, V. T.; Coon, J. B. *J. Mol. Spectrosc.* **1969**, 31, 137.
- (71) Lombardi, J. R. *J. Chem. Phys.* **1970**, 52, 6126.